

Non-monotonic Rheology and Stress Heterogeneity in Confined Granular Suspensions

Haitao Hu,¹ Yiqiu Zhao,¹ Weiwei Zhao,¹ Ligen Qiao,² and Qin Xu^{1,*}

¹*Department of Physics, The Hong Kong University of Science and Technology, Hong Kong, China*

²*Lushan New Materials Co., Ltd, Guangzhou, China*

(Dated: May 30, 2024)

We systematically investigated the impact of boundary confinement on the shear-thickening rheology of dense granular suspensions. Under highly confined conditions, dense suspensions were found to exhibit size-dependent or even rarely reported non-monotonic (*S*-shaped) flow curves in steady states. By performing *in-situ* boundary stress microscopy measurements, we observed enhanced flow heterogeneities in confined suspensions, where concentrated high-stress domains propagated stably either along or against the shear direction. By comparing the boundary stress microscopy results with macroscopic flow responses, we revealed the connection between non-monotonic rheology and stress heterogeneity in confined suspensions. These findings suggest the possibility of controlling suspension rheology by imposing different boundary confinements.

I. INTRODUCTION

Dense granular suspensions comprise concentrated non-Brownian particles mixed with a Newtonian liquid. They are omnipresent in diverse natural phenomena and engineering applications, including mudflows in landslides [1], construction materials [2], and field-responsive fluids [3, 4]. Unlike Newtonian fluids, the rheological response of a dense granular suspension to shear is often nonlinear. When suspension viscosity increases under shear, the flow behavior is referred to as shear thickening [5–7].

The physical mechanism of shear thickening can be understood across a hierarchy of length scales. Recent studies have interpreted shear thickening in dense non-Brownian suspensions has been interpreted as a shear-induced crossover from an unconstrained flow state to a constrained frictional state [8–10]. Within the shear-thickened flows, the suspended particles form direct contacts by overriding a critical stress, depending on the intrinsic interactions among particles [11, 12]. The continuous strengthening of large-scale contact networks results in a sharp increase in flow resistance [13, 14]. This phenomenological framework not only captures the essential characteristics of shear thickening in dense suspensions [11] but also predicts the emergence of *S*-shaped flow curves above a critical volume fraction [8, 15]. However, these non-monotonic rheological responses have rarely been observed in steady state measurements [16]. Instead, unstable flow instabilities and substantial stress fluctuations often dominates the flow responses in this regime [17–20].

Besides the multi-scale contact networks within dense suspensions, shear boundaries play essential roles in shear thickening. As dense suspensions tend to dilate under shear [21, 22], the shear plates apply positive normal stresses to stabilize the contact networks, enabling sustained thickening responses [11, 23]. Further, the geomet-

ric profiles of shear boundaries has been shown to control statistical features, including stress fluctuations [17] and flow heterogeneities [24–26], in dense suspensions. However, despite these experimental findings, the underlying mechanism by which the boundary conditions modulate the shear thickening flows remains unclear.

In this work, we systematically characterized the role of boundary confinement in both *sedimenting* and *non-sedimenting* granular suspensions. By combining rheological characterizations with boundary stress microscopy, we show that a strong confinement imposed by shear boundaries effectively stabilizes non-monotonic flow curves and induce local stress concentrations. Driven by the interplay between shear boundaries and particle interactions, the high-stress domains propagate dynamically, either along or against the shear direction. These emergent features of confined suspensions are greatly reduced when not confined.

II. MATERIALS

Athermal granular particles are commonly subjected to the influence of gravity. Therefore, particle-sedimentation plays an essential role in the rheological behaviors of many granular suspensions [17, 21, 27, 28]. On the other hand, for particles having polymeric components, it is possible to match their densities to that of the solvent [11, 12, 26, 29]. Non-sedimenting suspensions are usually stabilized by intrinsic inter-particle repulsions, such as electrostatic [30] and steric interactions [31]. In this study, we investigated the shear thickening rheology of both systems under confinement.

The non-sedimenting suspensions were prepared using polystyrene (PS) particles having a diameter of approximately $d_{ps} = 25 \mu\text{m}$, suspended in a glycerol-water mixture. The solvent made of 20 wt% glycerol dissolved in 80 wt% deionized water had a density of $\rho_{gw} = 1.05 \text{ g/cm}^3$, precisely matching that of PS particles, and a viscosity of approximately 1.75 cSt. The PS particles can be well dispersed and stabilized by electrostatic repulsions in the suspensions [32]. To demonstrate

* qinxu@ust.hk

this, we added sodium chloride (NaCl) to PS-glycerol suspensions. For a constant volume fraction of particles ($\phi = 60\%$), the yield stress rose as the salt concentration increased from 0.10 mol/L to 0.63 mol/L (Supplementary Fig. S1), confirming the role of charge stabilization in PS-glycerol suspensions.

The sedimenting suspensions were prepared by mixing glass beads ($d_g = 43\ \mu\text{m}$) with 20 cSt silicone oil. Due to the density difference between glass ($2.33\ \text{g}/\text{cm}^3$) and silicone ($0.95\ \text{g}/\text{cm}^3$), the particles were consistently affected by gravity. Thus, the glass particles sedimented in static states, leaving a thin fluid layer between the particles and the shear plate. As the shear stress increased, the particles gradually lifted against gravity [17, 21]. In this system, shear thickening occurred as the flow of particles spans across the whole shear gap [33].

III. SHEAR RHEOLOGY OF CONFINED SUSPENSIONS

Steady-state rheological measurements.— The shear rheology of both suspensions was characterized using an Anton Paar rheometer (MCR 302) equipped with a parallel-plate shear cell having a diameter of 43 mm (Fig. 1(a)). To prevent wall slippage, both shear plates were roughened using sandpapers (P-120 grade) with an average grain size of approximately $120\ \mu\text{m}$. We will show that these boundary conditions are essential to obtaining reliable rheological results [25, 26]. The shear stress (τ) was obtained from the torque T measured using the rheometer, according to

$$\tau = 4T/3\pi R^3, \quad (1)$$

where R is the radius of the shear plate. The shear rate was calculated from the angular velocity ω using

$$\dot{\gamma} = 2\omega R/(3h), \quad (2)$$

where h is the gap size. The viscosity of suspensions was defined by the ratio of shear stress to shear rate,

$$\eta = \tau/\dot{\gamma} = 2Th/\omega\pi R^4. \quad (3)$$

We simultaneously measured the normal force (F_N) applied to the shear plate, resulting in a normal stress

$$\tau_N = F_N/\pi R^2. \quad (4)$$

A positive normal stress ($\tau_N > 0$) indicates that the suspension pushes against the shear plate, whereas a negative normal stress ($\tau_N < 0$) indicates the opposite.

PS-water suspensions.— Figure 1(b) shows the flow curves of PS-water suspensions with $\phi = 0.60$, where the gap size was varied from $h = 1.65\ \text{mm}$ to $0.50\ \text{mm}$. For $h = 1.65\ \text{mm}$ (open left-triangles) and $h = 1.29\ \text{mm}$ (open circles), the suspension exhibited a Newtonian-like flow behavior, $\tau \sim \dot{\gamma}$, below a critical stress $\tau_{c1} \approx 6\ \text{Pa}$. For $\tau > \tau_{c1}$, $\tau(\dot{\gamma})$ displayed classical shear thickening

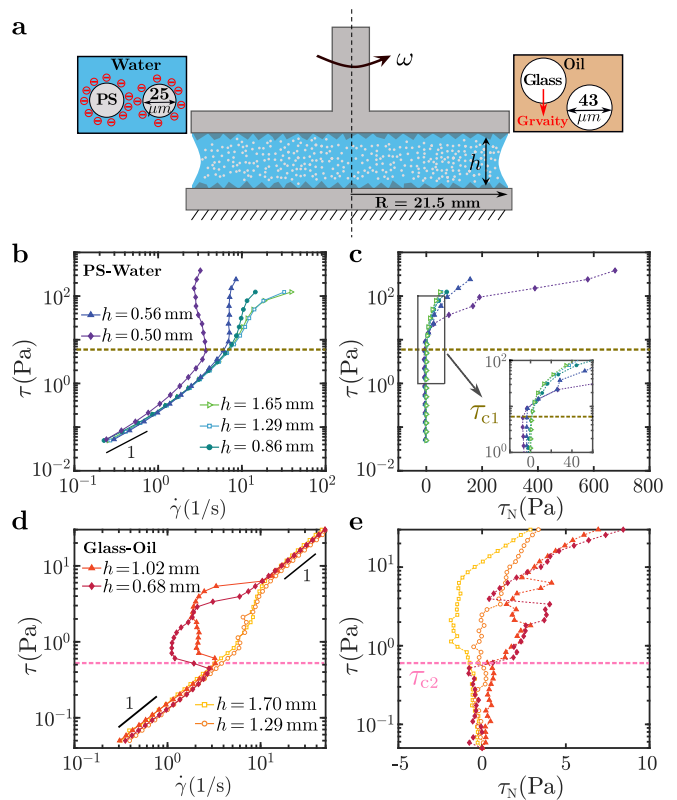


FIG. 1. Flow curves of confined dense suspensions. (a) Schematic illustration of the parallel-plate shear cell used to measure the shear rheology of dense granular suspensions. (b) Plots of shear stress (τ) against the shear rate ($\dot{\gamma}$) for the non-sedimenting PS-water suspensions at different gap sizes, namely $h = 1.65\ \text{mm}$, $1.29\ \text{mm}$, $0.86\ \text{mm}$, $0.56\ \text{mm}$, and $0.50\ \text{mm}$. (c) Plots of shear stress (τ) against the corresponding normal stress (τ_N) for the PS-water suspensions at the same gap sizes as in panel (b). The inset shows the same data near the onset of shear thickening (τ_{c1}) using expanded axes for clarity. (d) Plots of shear stress (τ) against shear rate ($\dot{\gamma}$) for the sedimenting glass-oil suspensions at different gap sizes, including $h = 1.70\ \text{mm}$, $1.29\ \text{mm}$, $1.02\ \text{mm}$, and $0.68\ \text{mm}$. (e) Plots of shear stress (τ) against the normal stress (τ_N) for the glass-oil suspensions at the same gap sizes shown in panel (d). The brown (panels (b) and (c)) and pink (panels (d) and (e)) dashed lines indicate the critical stresses (τ_{c1} and τ_{c2}) at which the S-shapes begin to emerge for the PS-water suspensions and glass-oil suspensions, respectively.

responses, where τ_{c1} is the stress required to establish direct contacts among PS particles by overcoming the electrostatic repulsion.

By further decreasing the gap size, we obtained size-dependent flow curves. For instance, the suspensions shear-thicken more profoundly under $h = 0.86\ \text{mm}$ (solid circles), and even discontinuously at $h = 0.56\ \text{mm}$ (solid up-triangles). More strikingly, a non-monotonic flow curve of $\tau(\dot{\gamma})$ appeared as h became as small as $0.50\ \text{mm}$ (solid diamonds), where a flow regime with a negative slope, $d\tau/d\dot{\gamma} < 0$, emerges above τ_c .

In addition, the increase in the viscosity of PS-water

suspensions was associated with a synchronous rise of the normal stress (τ_N). As shown in Fig. 1(c), τ_N appears positive and increases with τ above $\tau_{c1} \approx 6$ Pa in all the measurements. For the suspensions with $h = 0.56$ mm and 0.50 mm, containing approximately 20 layers of PS particles, the increase in τ_N due to thickening-induced dilation became appreciable. Given that τ_N scales almost linearly with τ under highly confined conditions (Supplementary Fig. S2), we conjecture that the discontinuous and non-monotonic flow curves in Fig. 1(b) emerge as the system size approaches the correlation length scale of frictional contact networks in the sheared PS-water suspensions.

Glass-oil suspensions.— We further characterized the rheology of sedimenting glass-oil suspensions as the gap size was varied from $h = 1.70$ mm to 0.68 mm. Due to the slow relaxation dynamics of the glass particles in viscous silicone oil, the shear rate $\dot{\gamma}$ at each shear stress τ was obtained by averaging the instantaneous values over a period of $t_w = 200$ s. As a further increase in t_w did not vary the flow curves (Supplementary Fig. S3), we conclude that the resulting $\tau(\dot{\gamma})$ represented the flow curves at steady states. Figure 1(d) shows $\tau(\dot{\gamma})$ of the glass-oil suspensions with $\phi = 52$ % measured at different h . For each individual trace, we identified two distinctive Newtonian regimes at $\tau < \tau_{c2} = 0.5$ Pa and $\tau > \tau_e = 6$ Pa, respectively. The crossover between the two flow regimes represents a shear thickening transition from a sedimenting to a suspended flow state. As τ_{c2} is consistent with the gravitational stress $\Delta\rho g d_g \approx 0.58$ Pa where $\Delta\rho$ is the density difference between the glass and silicone oil, shear thickening in glass-oil suspensions was initiated by rearranging the particle configurations against sedimentation [17, 21]. Similar to the PS-water suspensions, S -shaped flow curves for glass-oil suspensions emerged as the gap size was reduced to ~ 20 particle diameters: for $h = 1.02$ mm and 0.68 mm, $\tau(\dot{\gamma})$ becomes non-monotonic between τ_{c2} and τ_e , with τ_N rising more drastically than for large gaps (Fig. 1(e)).

Stability of the S-shaped flow curves.— As the shear stress τ was ramped up and down cyclically, we observed negligible hysteresis of $\tau(\dot{\gamma})$ in the PS-water suspensions (Supplementary Fig. S4(a)). In contrast, for glass-oil suspensions under cyclic testing, the S -shaped traces still remained qualitatively unchanged although the hysteresis loops emerged (Supplementary Fig. S4(b)). These observations suggest that the non-monotonic flow curves, which have been rarely observed in experiments [16], were stabilized by the imposed confinements. This mechanical stability is consistent with predictions in a previous simulation [34]: a confined suspension can potentially enhance particle contacts while reducing the shear rate, in response to an increasing shear stress.

We further examined the role of boundary roughness in the non-monotonic responses. Using a shear plate roughened by a finer sand paper (grain size ≈ 50 μm), the S -shaped flow curves of PS-water suspensions disappeared at $h = 0.50$ mm and then re-emerged as h was further re-

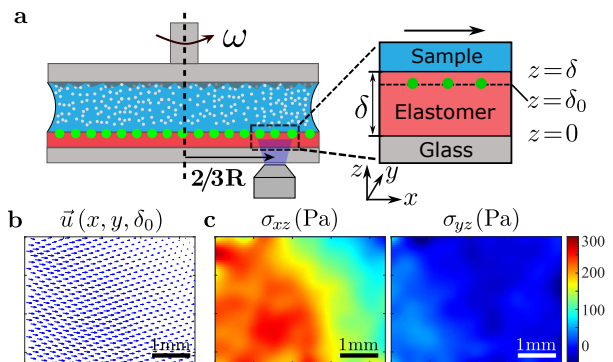


FIG. 2. **Boundary stress microscopy (BSM).** (a) Schematic illustration of the boundary stress microscopy incorporated into the parallel-plate shear cell. A film of soft silicone gel coated with fluorescent nanobeads was attached on the bottom shear plate. (b) Representative displacement fields $\vec{u}(x, y)$, and stress maps σ_{xz} and σ_{yz} measured by BSM.

duced to 0.33 mm (Supplementary Fig. S5(a)). This observation suggests the essential roles of boundary roughness in stabilizing non-monotonic flows in the PS-water suspensions. With a reduced boundary roughness, wall slips can destabilize non-monotonic flows [35]. In contrast, the S -shaped flow curves in confined glass-oil suspensions have a negligible dependence on the boundary roughness (Supplementary Fig. S5(b)). As the glass particles are constantly affected by gravity, the shear plate is more likely to be in contact with the solvent film than with the particles, such that wall slips are prevented regardless of the boundary roughness.

IV. LOCAL SHEAR STRESS FLUCTUATIONS

Boundary stress microscopy.— To search for the underlying origin of the non-monotonic behaviors, we employed boundary stress microscopy (BSM) to characterize the shear-induced heterogeneity in confined suspensions. This technique was initially developed to measure in-plane tractions at soft interfaces [36, 37], and was later improved for *in-situ* measurements of boundary stresses in rheological characterizations [38, 39]. Below, we briefly summarize the theoretical and experimental methods used in the BSM analysis.

To perform BSM, we coated a layer of soft gels with a Young's modulus E and a thickness δ_0 on the bottom plate of the shear cell. We characterized the local shear stresses at the boundaries of suspensions by measuring the deformations of this soft substrate. Considering linear elasticity, the constitutive relation between stress $\boldsymbol{\sigma}$ and displacement \mathbf{u} of soft gels is expressed as

$$\boldsymbol{\sigma} = \frac{E}{1+\nu} \left(\frac{1}{2} (\nabla \mathbf{u} + \nabla \mathbf{u}^T) + \frac{\nu \nabla \cdot \mathbf{u}}{1-2\nu} \mathbf{I} \right), \quad (5)$$

where ν is Poisson's ratio of the soft layer and \mathbf{I} is the unity matrix. In addition, the mechanical equilibrium

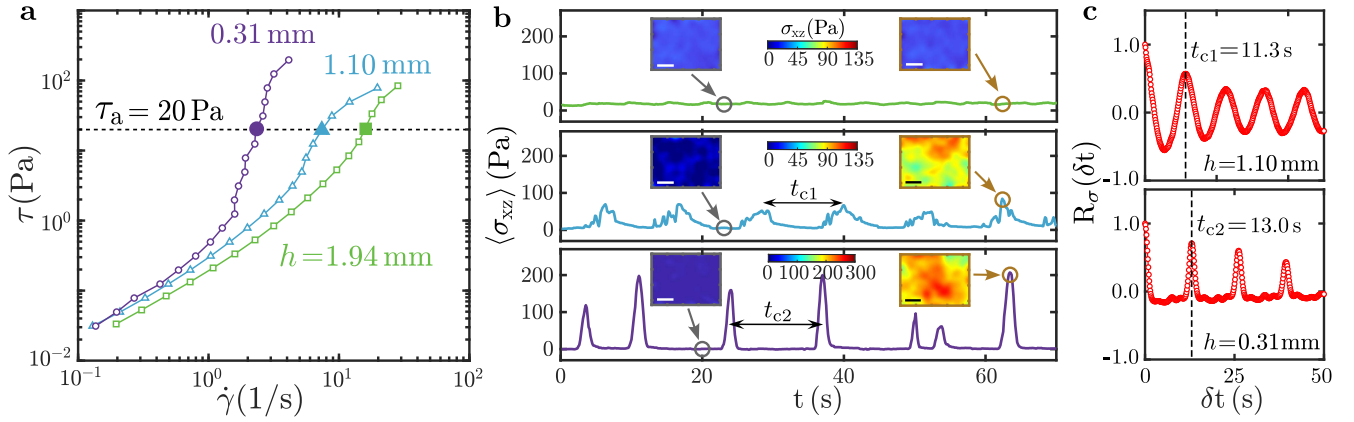


FIG. 3. **Local stress fluctuations in PS-water suspensions.** (a) Flow curves of the PS-water suspensions measured with the BSM setup at $h = 1.94$ mm, 1.10 mm, and 0.31 mm. (b) Temporal fluctuations of $\langle\sigma_{xz}(t)\rangle$ measured at $\tau_a = 20$ Pa for the gap sizes $h = 1.94$ mm (green), 1.10 mm (blue), and 0.31 mm (purple). The characteristic timescales t_{c1} and t_{c2} represent the time intervals between two high-stress events. The insets show the stress map (σ_{xz}) at the time points indicated by the open circles. Scale bars: 1000 μm . (c) Autocorrelation function $R_\sigma(\delta t)$ for $h = 1.10$ mm and 0.31 mm.

within the soft layer is governed by

$$(1 - 2\nu)\nabla^2\mathbf{u} + \nabla(\nabla \cdot \mathbf{u}) = 0 \quad (6)$$

with the boundary conditions

$$\mathbf{u}|_{z=\delta} = (u_x^*, u_y^*, 0) \text{ and } \mathbf{u}|_{z=0} = (0, 0, 0), \quad (7)$$

where (u_x^*, u_y^*) represents the in-plane displacements on the upper surface of the soft layer ($z = h$), whereas the bottom surface is always undeformed ($z = 0$). As depicted in Fig. 2(a), x and y are the shear and vorticity directions, respectively, and z is the gradient direction. By applying Fourier transformations to both the stress and displacement fields, $\sigma_{ij} = \int \hat{\sigma}_{ij} \exp[i(k_x x + k_y y)] dk_x dk_y$ and $u_i = \int \hat{u}_i \exp[i(k_x x + k_y y)] dk_x dk_y$ where $i, j = x, y, z$, we obtain the relationship between stress and displacement in Fourier space

$$\hat{\sigma}_{iz}(k_x, k_y, z) = \mathbf{Q}_{ij}(k_x, k_y, z) \hat{u}_j(k_x, k_y, z), \quad (i = x, y), \quad (8)$$

where the explicit form of the matrix \mathbf{Q} is provided in the Supplementary Information. As the surface displacements u_x^* and u_y^* are measured experimentally, we quantitatively determine the elastic stresses (σ_{xz} and σ_{yz}) at $z = \delta_0$ using Eq. 8 (Fig. 2(a)). For each stress map obtained by BSM, we denote $\langle\sigma_{iz}\rangle$ as the spatially averaged σ_{iz} over the field of view.

The soft layers in our BSM setup were made of polydimethylsiloxane gels (PDMS from DMS-V31, Gelest Inc.) crosslinked by trimethylsiloxane copolymers (HMS-301, Gelest Inc.), with a Poisson's ratio $\nu = 0.48$ [40]. The gel thickness was determined by the spin-coating speed applied to uncrosslinked PDMS mixtures, and the Young's modulus of a cured gel was controlled by the weight ratio of crosslinkers (k). We deposited a layer of 5 μm fluorescent beads on the PDMS surfaces as tracers to measure u_x^* and u_y^* and to quantify the boundary stresses σ_{xz} and σ_{yz} using Eq. 8. The objective was

placed at a distance of $2R/3$ from the plate center, where the local shear rate was identical to the average shear rate measured by the rheometer (Eq. 2). The imaging speed was controlled between 3.8 frames per second and 7.6 frames per second, which was high enough to capture the evolving stress heterogeneity. As σ_{xz} remained substantially larger than σ_{yz} in all our experiments (Fig. 2(b) and Supplementary Figs. S6 and S7), we focused only on the evolution of σ_{xz} in this study.

To characterize the PS-water suspensions, we chose $k = 0.97\%$, $E = 7.5$ kPa, and a gel thickness $\delta_0 = 80$ μm . During the shear thickening transition, the average shear stresses ($\sim 10^1$ Pa) were large enough to remove the nanobeads from gel surfaces. To prevent this, we added an additional PDMS film with a thickness of 6 μm on the top (Fig. 2(a)), such that the gel surface (δ) was slightly higher than the plane of nanobeads (δ_0). We used σ_{iz} ($i = x, y$) at $z = \delta_0$ to estimate the boundary stress induced by the PS-water suspensions.

In contrast, the shear stresses in glass-oil suspensions were only $\sim 10^0$ Pa, substantially lower than those of PS-water suspensions. We thus chose $k = 0.81\%$ and no additional PDMS film was needed above the nano-beads ($\delta = \delta_0 = 80$ μm). To prevent the swelling effects due to the oil component in solvents, we swelled the gel layers with a 20 cSt silicone oil before the experiments. Consequently, the fully swollen PDMS layer has a thickness of 92 μm and a Young's modulus of $E = 1.7$ kPa.

Ps-water suspensions. — In the BSM setup, the boundary roughness decreased due to the presence of a soft layer on the bottom plate. Consequently, although size-dependent flow curves of PS-water suspensions still emerged at $h \leq 1.10$ mm, there were no non-monotonic behaviors even at $h = 0.31$ mm, as shown in Fig. 3(a). This result is consistent with our aforementioned observation that the rheology of PS-water suspensions is sensitive to boundary roughness. As the size-dependent

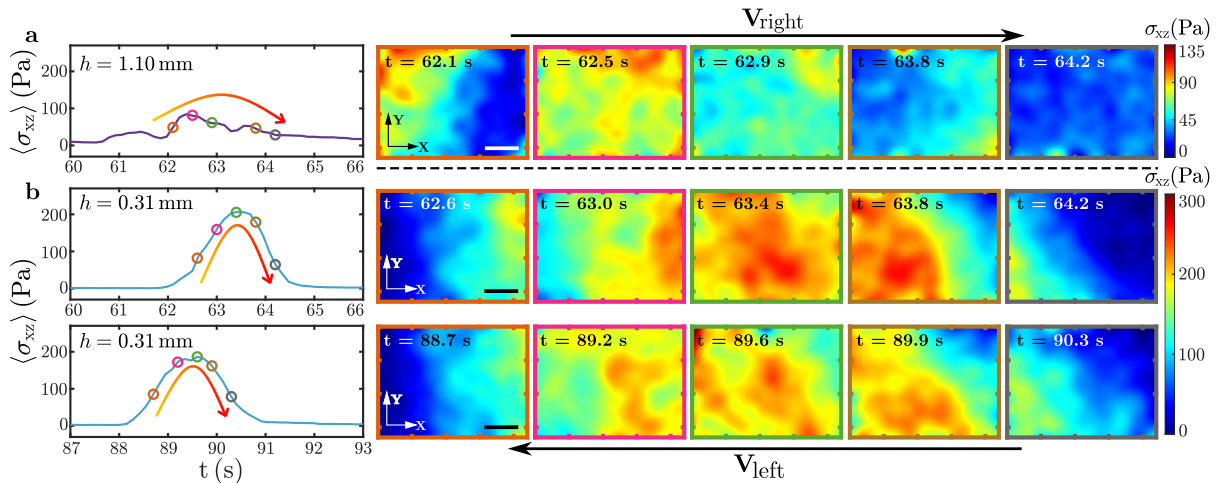


FIG. 4. **Propagation of high-stress regions in PS-water suspensions for (a) $h = 1.10$ mm and (b) $h = 0.31$ mm.** Left panels: representative peaks of $\langle \sigma_{xz}(t) \rangle$ at $\tau_a = 20$ Pa. Right panel: stress maps of σ_{xz} at different times indicated by the open circles in the left panels. Scale bars: $1000 \mu\text{m}$.

rheology is the precursor of non-monotonic flow curves (Fig. 1), we conjecture that the boundary stresses characterized in this regime ($h \leq 1.10$ mm) remain important indicators of the local flows in non-monotonic regimes.

By maintaining a constant shear stress $\tau_a = 20$ Pa in the thickening regime, we performed BSM measurements to characterize the evolution of local flows at $h = 0.31$ mm, 1.10 mm, and 1.94 mm. Figure 3(c) shows that $\langle \sigma_{xz}(t) \rangle$ remains steady at $h = 1.94$ mm, but significantly fluctuates between a dominating low-stress state and a series of high-stress peaks under both $h = 1.10$ mm and 0.31 mm. The peak stresses of $\langle \sigma_{xz}(t) \rangle$ at $h = 0.31$ mm are close to 200 Pa, approximately twice those at $h = 1.10$ mm, suggesting that the size-dependent flow curves were associated with enhanced flow heterogeneity.

We further characterized the temporal intervals between adjacent high-stress spikes of $\langle \sigma_{xz}(t) \rangle$ at $h = 1.10$ mm and 0.31 mm. To quantify the characteristic timescale (t_c), we consider the autocorrelation function

$$R_\sigma(\delta t) = \frac{\mathbf{E}[\langle \sigma_{xz}(t) \rangle \langle \sigma_{xz}(t + \delta t) \rangle]}{\mathbf{E}[\langle \sigma_{xz}(t) \rangle^2]} = \frac{\int_0^T \langle \sigma_{xz}(t) \rangle \langle \sigma_{xz}(t + \delta t) \rangle dt}{\int_0^T [\langle \sigma_{xz}(t) \rangle]^2 dt} \quad (9)$$

where T is the total measurement period. When $\delta t = t_c$, we expect a local maximum in the plot of $R_\sigma(\delta t)$. Figure 3(c) shows the plots of $R_\sigma(\delta t)$ with the primary peaks at $t_{c1} = 11.3$ s and $t_{c2} = 13.0$ s for $h = 1.10$ mm and 0.31 mm. These two timescales well captures the time intervals between high-stress peaks presented in Fig. 3(b). Given the rotational period of the shear plate $T_g = 4\pi R/(3\dot{\gamma}h)$, we found

$$t_{c1} \approx T_g, \quad t_{c2} \approx T_g/10. \quad (10)$$

The relationships between $t_{c1(2)}$ and T_g in Eq. 10 are important for understanding the underlying mechanisms of flow heterogeneity due to confinement. At $h = 1.10$ mm, the approximate equality between t_{c1} and T_g aligns well with previous findings for the discontinuous shear-thickening of cornstarch-water suspensions [39, 41]. However, the fast timescale t_{c2} observed under the highly confined condition, $h = 0.31$ mm, has not been reported.

To address the difference between t_{c1} and t_{c2} , we investigated the propagations of local high-stress domains. Figure 4 shows the snapshots of σ_{xz} evolving during representative high-stress events for the two gap sizes. At $h = 1.10$ mm, a millimeter-sized high-stress front emerges from the left, and then moves rightward to cross the imaging field (Fig. 4(a) and Supplementary Video 1), aligning with the shear direction. In contrast, we observed reversed propagations of high-stress regions at $h = 0.31$ mm, with these regions initially appearing from the right and then traveling to the left, as shown in Fig 4(b) for two typical events (Supplementary Video S2). This counter-shear propagation with a traveling period ($t_{c2} \approx T_g/10$) was common for $h < 0.5$ mm. Compared with previous observations in cornstarch-water suspensions [28, 39], the counter-flow of high-stress regions was more stable in confined PS-water suspensions.

As illustrated in Fig. 5, we propose two flow mechanisms to interpret the propagations of high-stress domains in different directions. For the PS-water suspensions at $h = 1.10$ mm, we conjecture that a locally jammed, solid-like particle aggregation moves along the shear direction (Fig. 5(a)). Under no-slip boundary conditions, the propagation speed of this particle aggregation remains close to that of the shear plate. Consequently, a high-stress domain emerges once every rotational period ($t_{c1} \approx T_g$) [41]. In contrast, we speculate that the counter-flow propagation at $h = 0.31$ mm is associated with a simultaneous accumulation-release process

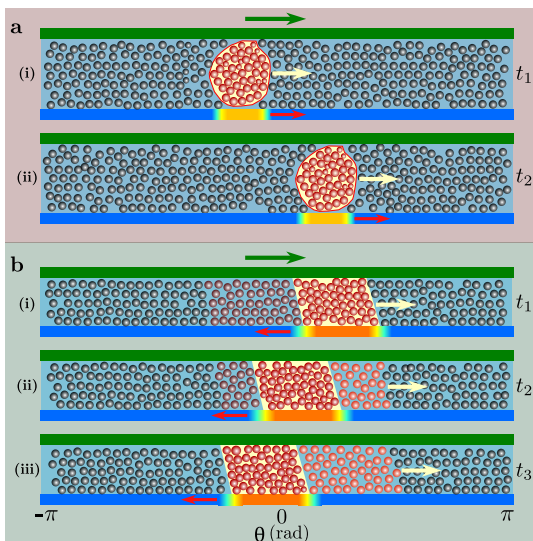


FIG. 5. **Schematic illustrations of propagating high-stress domains in confined suspensions.** (a) A particle aggregation (red spheres) travels along the shear direction. If the aggregation remains anchored to the top plate, the particles travel together at the same speed (e.g., the case of PS-water suspensions at $h = 1.10$ mm). If the aggregation travels along the centerline of the gap, its propagation speed is approximately half that of the shear plate (e.g., the case of glass-oil suspensions). (b) Under highly confined conditions, a particle aggregation may be partially jammed by the gap. As the top plate continues to shear, the particles at the leading front move forward, and consequently disengage from the aggregation. Meanwhile, the particles trailing behind join the aggregation. This dynamic release-accumulation process leads to a counter-flow propagation of high-stress regions (e.g., the case of PS-water suspensions at $h = 0.31$ mm).

of particle aggregations. As illustrated by Fig. 5(b), the particle aggregations can be partially jammed by confinement at $h = 0.31$ mm. While the particles at the leading front migrate forward and gradually separate from the aggregation (yellow arrows in Fig. 5(b)), the trailing particles are stopped by this locally jammed region (red arrows in Fig. 5(b)), which results in a propagation of high-stress regions against the shear direction. As this backward propagation of boundary stresses is determined by the particle-density, the propagation speed can be significantly higher than that of the shear plate ($t_{c2} \approx T_g/10$). In both scenarios (Figs. 5(a) and (b)), we expect enhanced local dilations of the high-stress domains [28, 41].

Glass-oil suspensions.— We further performed BSM measurements on glass-oil suspensions. Since the rheological behaviors of glass-oil suspensions were insensitive to the boundary roughness (Sec. III and Supplementary Fig. S5(b)), the non-monotonic flow curves remained unchanged in the BSM setup (Fig. 6(a)). The material properties of glass-oil suspensions have two advantages for BSM characterization: (1) the non-volatile solvent allows *in-situ* measurements over a long period, and (2) the

glass-oil suspensions exhibits a broader shear-thickening range than the PS-water suspensions. Thus, for glass-oil suspensions, we were able to conduct BSM measurements by systematically varying the shear stress within shear thickening regime.

Figure 6(a) shows that the non-monotonic flows of glass-oil suspensions emerges as the gap size decreases from $h = 1.68$ mm to $h = 0.87$ mm in the BSM setup. We maintained the global shear stress constant at $\tau_a = 1$ Pa, 2 Pa, 3 Pa, 4 Pa, and 6 Pa, respectively. Figure 6(b) presents the temporal evolutions of the averaged local stress $\langle \sigma_{xz} \rangle$ under the confined condition, $h = 0.87$ mm. Similar to PS-water suspensions, the local stress $\langle \sigma_{xz} \rangle$ in glass-oil suspensions also fluctuates between a nearly zero-stress state and a series of high-stress peaks within the non-monotonic regime. As τ_a increases from 1 Pa to 4 Pa, the high-stress peaks gradually rise from 15 Pa to 30 Pa. Representative stress maps are shown in Fig. 6(c). However, as τ_a further increases to 6 Pa, the flow heterogeneity notably reduces and σ_{xz} remains constant around 7.8 Pa (Supplementary Video S4). We interpret this homogenization of shear flows at $\tau_a = 6$ Pa as a dynamic yielding process in that the high-stress domains relax under shear. Consequently, this process substantially reduces flow resistance (Fig. 6(a)) and decreases normal stresses sharply (Fig. 1(e)).

At a large gap size $h = 1.68$ mm, the local stress fluctuations remain insignificant throughout the shear thickening regime, and the BSM measurements show a nearly homogenous shear flow (Supplementary Fig. S7). These findings further confirm that the flow heterogeneity depicted in Fig. 6 was induced by boundary confinement.

Using the autocorrelation analysis employed in Eq. 9, we quantified the characteristic timescales between two consecutive high-stress peaks for confined glass-oil suspensions ($h = 0.87$ mm). Figure 7(a) represents the results of R_σ evaluated at $\tau_a = 1$ Pa, 3 Pa, and 4 Pa. When $\tau_a = 1$ Pa, the first peak in $R_\sigma(\delta t)$ is located at $\delta t = 192$ s, which well approximates the time interval between two adjacent peaks (t'_{c1}) in Fig. 7(b). For $\tau_a = 3$ Pa and 4 Pa, $\langle \sigma_{xz}(t) \rangle$ oscillates more rapidly with two distinct timescales. For example, we observed a local maximum at $\delta t = 62$ s followed by a major peak at $\delta t = 104$ s. As shown in Fig. 7(b), the longer timescale corresponds to the intervals between two major peaks ($t'_{c1} \approx 106$ s), whereas the shorter timescale approximates a sub-interval between a lower spike and a major peak ($t'_{c2} \approx 62$ s). The two intervals are indicated by the black and pink arrows.

We further compared both t'_{c1} and t'_{c2} with the rotational period T_g . Figure 7(c) shows the plots of both t'_{c1} and t'_{c2} against T_g . For $\tau_a = 1$ Pa and 2 Pa, only the timescale of t'_{c1} was identified in the autocorrelation analysis. In contrast, for $\tau_a = 3$ Pa and 4 Pa, both t'_{c1} and t'_{c2} appear in the plots of $R_\sigma(\delta t)$. The results in Fig. 7(c) indicate two linear scalings,

$$t'_{c1} \approx 2T_g, \quad t'_{c2} \approx T_g. \quad (11)$$

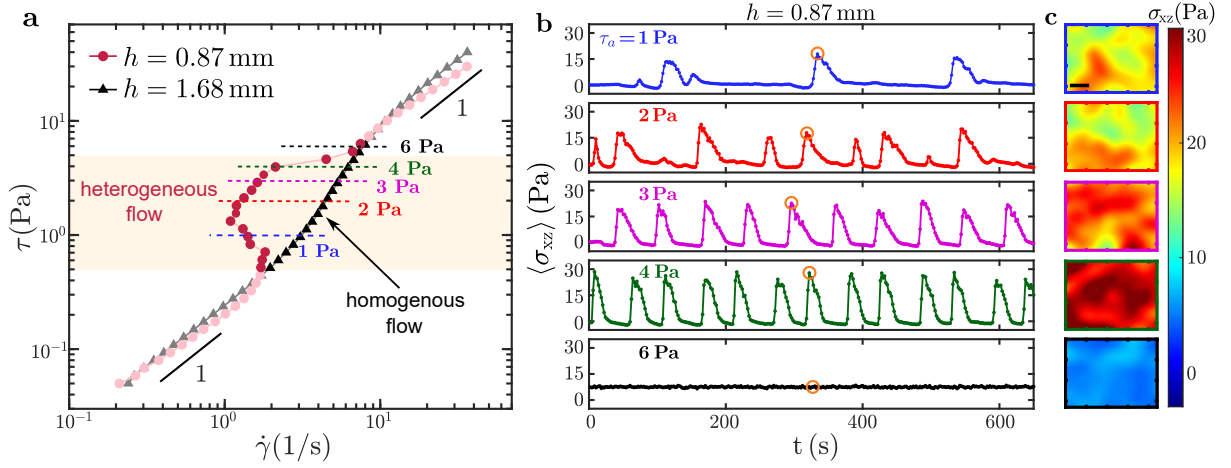


FIG. 6. **Local stress fluctuations in glass-oil suspensions.** (a) Flow curves measured with the BSM setup for $h = 1.68$ and 0.87 mm, respectively. The dashed lines indicate the shear stresses (τ_a) that we applied to suspensions while conducting long-period BSM measurements. (b) Temporal fluctuations of $\langle \sigma_{xz}(t) \rangle$ at $\tau_a = 1$ Pa, 2 Pa, 3 Pa, 4 Pa, and 6 Pa for $h = 0.87$ mm. (c) Local stress maps (σ_{xz}) at the times indicated by the open circles in (b). Scale bars: $200 \mu\text{m}$.

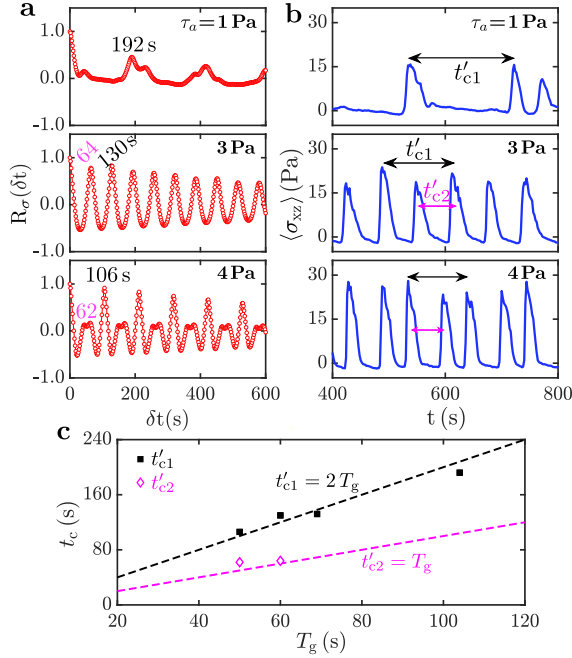


FIG. 7. **Fluctuation timescales of local shear stress (σ_{xz}) in confined glass-oil suspensions.** (a) Autocorrelation functions $R_\sigma(\delta t)$ at $\tau_a = 1$ Pa, 3 Pa, and 4 Pa for $h = 0.87$ mm. (b) Plots of $\langle \sigma_{xz}(t) \rangle$ at $\tau_a = 1$ Pa, 3 Pa, and 4 Pa. The two characteristic timescales, t'_{c1} and t'_{c2} , are indicated by the black and pink arrows, respectively. (c) Plots of t'_{c1} and t'_{c2} against the rotational period of the shear plate (T_g).

In contrast with the characteristic timescales measured for the PS-water suspensions (Eq. 10), the ultra-fast propagating mode ($\sim T_g/10$) was not observed in the glass-oil suspensions (Eq. 11).

To interpret the timescales t'_{c1} and t'_{c2} , we also mea-

sured the dynamics of the high-stress domains in the confined glass-oil suspensions. Figure 8 shows the propagation of representative high-stress domains for $\tau_a = 1$ Pa and 4 Pa, respectively. These local domains always travel in the same direction as the shear plate, and no counter-flow propagation was observed in any experiments (Supplementary Videos S5). We conjecture that the simultaneous accumulation and release of high-stress domains (as illustrated in Fig. 5(b)) are absent in glass-oil suspensions due to the relatively weak stress localizations ($\langle \sigma_{xz} \rangle < 30$ Pa) in the non-monotonic regime.

We herein interpret the dependence of t'_{c1} and t'_{c2} on T_g (Eq. 11) based on the flow mechanisms shown in Fig. 5(a). When $\tau_a = 1$ Pa or 2 Pa, briefly exceeding the onset of shear thickening, a local particle aggregation forms in the suspensions. Due to the weak boundary stresses ($\langle \sigma_{xz} \rangle < 30$ Pa), the particle aggregation possibly travels along the center of the shear cell without sticking to the shear plate [24]. The mean traveling speed of the aggregation is approximately half that of the shear plate, such that the high-stress region finishes one complete round during two rotational periods, $t'_{c1} \approx 2T_g$. For $\tau_a = 3$ Pa or 4 Pa, a second high-stress domain can appear in a different location within the suspension. We thus observed the high-stress regions twice as frequently as we did at lower stresses, leading to $t'_{c2} \approx T_g$.

V. CONCLUSIONS

By systematically characterizing the shear thickening behaviors of both non-sedimenting PS-water suspensions and sedimenting glass-oil suspensions, we have demonstrated the critical role of boundary confinement in determining shear thickening rheology. The major findings of this work are summarized as follows.

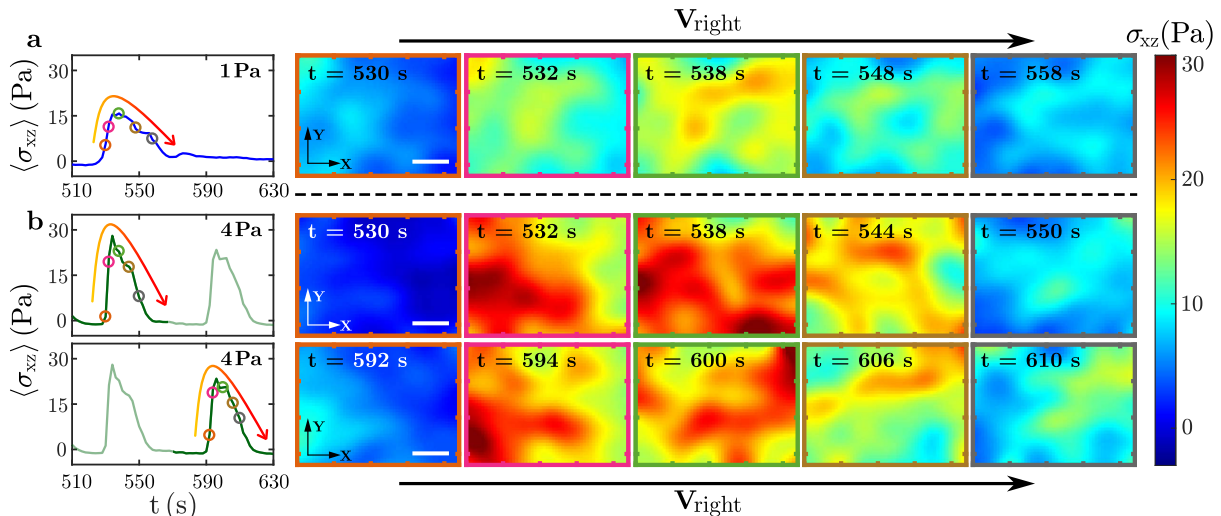


FIG. 8. **Propagation of high-stress regions in confined glass-oil suspensions at (a) $\tau_a = 1$ Pa and (b) $\tau_a = 4$ Pa.** Left panels: representative peaks of $\langle \sigma_{xz}(t) \rangle$ at $h = 0.87$ mm. Right panels: stress maps of σ_{xz} at different times indicated by the open circles in the left panels. Scale bars: $200 \mu\text{m}$.

(1) Although non-monotonic flow curves have been predicted theoretically, they have rarely been reported in previous experiments due to flow instabilities [35, 42]. Our results show that strong confinement imposed by a shear boundary can effectively induce stable *S*-shaped responses in the shear thickening regime (Fig. 1). Although high-stress domains develop in the non-monotonic regimes, boundary confinement prevents the stress heterogeneity from evolving into large-scale rheochaos [28].

(2) Using boundary stress microscopy (BSM) (Fig. 2), we characterized the rich dynamics of local stress heterogeneity induced by boundary confinement. For both PS-water and glass-oil suspensions, we observed the propagations of high-stress domains at speeds controlled by the rotational shear plate (Eqs. 10 and 11). For PS-water suspensions, we observed a crossover from the shear-directed to counter-shear propagations of high-stress domains as the gap size reduced (Fig. 4). While both propagation directions have previously been reported in dense suspensions [24, 28, 38, 39, 43], we demonstrated that these local high-stress domains remain stable under confinement. Intriguingly, the counter-shear propagation in PS-water suspensions appears to be significantly faster than the rotation of the shear plate (Eq. 10), potentially caused by a simultaneous accumulation-release process of high-stress aggregations (Fig. 5(b)). For glass-oil suspensions, however, the high-stress domains always propagate along the shear direction, regardless of the gap size (Fig. 8). The absence of counter-shear propagation is possibly attributed to the weak boundary stresses ($\sigma_{xz} \sim 30$ Pa) induced in confined glass-oil suspensions.

(3) The rheology of PS-water suspensions depends on

the material properties of shear boundaries. With shear plates made of roughened glass, *S*-shaped flow curves appeared for confined PS-water suspensions (Fig. 1(b)). However, when a gel film was coated on the bottom plate for BSM measurements, the flow curves were consistently monotonic even under strong confinement (Fig. 3(a)). We attribute this absence of non-monotonic responses to the smoothness of gel surfaces and the deformations of gel films under large boundary stresses ($\sigma_{xz} \sim 300$ Pa) in confined PS-water suspensions.

In summary, we presented an experimental investigation that revealed the underlying connection between shear thickening rheology and local flow structures in confined dense suspensions. We have demonstrated that boundary confinements can effectively stabilize *S*-shaped flow curves and induce local stress heterogeneity. Our results provide valuable insights into controlling suspension rheology through boundary effects.

ACKNOWLEDGEMENT

We thank Prof. Ryohei Seto for valuable suggestions. This work was supported by the Early Research Scheme (26309620), General Research Funds (No.16307422 and No.16305821), and the Collaborative Research Fund (No.CY6004-22Y) from the Hong Kong Research Grants Council. The research activities were also funded by the Partnership Seed Fund (No.ASPIRE2021#1) from the Asian Science and Technology Pioneering Institutes of Research and Education League and Hong Kong-Macau-Guangdong Industrialization Fund from Guangdong Science and Technology Department (No.2023A0505030017).

-
- [1] Fabio Vittorio De Blasio, “Rheology of a wet, fragmenting granular flow and the riddle of the anomalous friction of large rock avalanches,” *Granular Matter* **11**, 179 (2009).
- [2] Abhay Goyal, Ivan Palaia, Katerina Ioannidou, Franz-Josef Ulm, Henri van Damme, Roland J.-M. Pellenq, Emmanuel Trizac, and Emanuela Del Gado, “The physics of cement cohesion,” *Science Advances* **7**, eabg5882 (2021).
- [3] Juan de Vicente, Daniel J. Klingenberg, and Roque Hidalgo-Alvarez, “Magnetorheological fluids: a review,” *Soft Matter* **7**, 3701–3710 (2011).
- [4] Wing Yim Tam, Guang Hua Yi, Weijia Wen, Hongru Ma, M. M. T. Loy, and Ping Sheng, “New electrorheological fluid: Theory and experiment,” *Phys. Rev. Lett.* **78**, 2987–2990 (1997).
- [5] Jeffrey F. Morris, “Shear thickening of concentrated suspensions: Recent developments and relation to other phenomena,” *Annual Review of Fluid Mechanics* **52**, 121–144 (2020).
- [6] Eric Brown and Heinrich M Jaeger, “Shear thickening in concentrated suspensions: phenomenology, mechanisms and relations to jamming,” *Reports on Progress in Physics* **77**, 046602 (2014).
- [7] Christopher Ness, Ryohei Seto, and Romain Mari, “The physics of dense suspensions,” *Annual Review of Condensed Matter Physics* **13**, 97–117 (2022).
- [8] M. Wyart and M. E. Cates, “Discontinuous shear thickening without inertia in dense non-brownian suspensions,” *Phys. Rev. Lett.* **112**, 098302 (2014).
- [9] Romain Mari, Ryohei Seto, Jeffrey F. Morris, and Morton M. Denn, “Discontinuous shear thickening in brownian suspensions by dynamic simulation,” *Proceedings of the National Academy of Sciences* **112**, 15326–15330 (2015).
- [10] B. M. Guy, M. Hermes, and W. C. K. Poon, “Towards a unified description of the rheology of hard-particle suspensions,” *Phys. Rev. Lett.* **115**, 088304 (2015).
- [11] John R. Royer, Daniel L. Blair, and Steven D. Hudson, “Rheological signature of frictional interactions in shear thickening suspensions,” *Phys. Rev. Lett.* **116**, 188301 (2016).
- [12] Nayoung Park, Vikram Rathee, Daniel L. Blair, and Jacinta C. Conrad, “Contact networks enhance shear thickening in attractive colloid-polymer mixtures,” *Phys. Rev. Lett.* **122**, 228003 (2019).
- [13] Romain Mari and Ryohei Seto, “Force transmission and the order parameter of shear thickening,” *Soft Matter* **15**, 6650–6659 (2019).
- [14] Shravan Pradeep, Mohammad Nabizadeh, Alan R. Jacob, Safa Jamali, and Lilian C. Hsiao, “Jamming distance dictates colloidal shear thickening,” *Phys. Rev. Lett.* **127**, 158002 (2021).
- [15] Romain Mari, Ryohei Seto, Jeffrey F. Morris, and Morton M. Denn, “Nonmonotonic flow curves of shear thickening suspensions,” *Phys. Rev. E* **91**, 052302 (2015).
- [16] Zhongcheng Pan, Henri de Cagny, Bart Weber, and Daniel Bonn, “S-shaped flow curves of shear thickening suspensions: Direct observation of frictional rheology,” *Phys. Rev. E* **92**, 032202 (2015).
- [17] Qin Xu, Abhinendra Singh, and Heinrich M. Jaeger, “Stress fluctuations and shear thickening in dense granular suspensions,” *Journal of Rheology* **64**, 321–328 (2020).
- [18] Rijan Maharjan, Ethan O’Reilly, Thomas Postiglione, Nikita Klimenko, and Eric Brown, “Relation between dilation and stress fluctuations in discontinuous shear thickening suspensions,” *Phys. Rev. E* **103**, 012603 (2021).
- [19] Didier Lootens, Henri Van Damme, and Pascal Hébraud, “Giant stress fluctuations at the jamming transition,” *Phys. Rev. Lett.* **90**, 178301 (2003).
- [20] Omer Sedes, Abhinendra Singh, and Jeffrey F. Morris, “Fluctuations at the onset of discontinuous shear thickening in a suspension,” *Journal of Rheology* **64**, 309–319 (2020).
- [21] Eric Brown and Heinrich M. Jaeger, “The role of dilation and confining stresses in shear thickening of dense suspensions,” *Journal of Rheology* **56**, 875–923 (2012).
- [22] Qin Xu, Sayantan Majumdar, Eric Brown, and Heinrich M. Jaeger, “Shear thickening in highly viscous granular suspensions,” *Europhysics Letters* **107**, 68004 (2014).
- [23] Ryohei Seto and Giulio G. Giusteri, “Normal stress differences in dense suspensions,” *Journal of Fluid Mechanics* **857**, 200–215 (2018).
- [24] Guillaume Ovarlez, Anh Vu Nguyen Le, Wilbert J. Smit, Abdoulaye Fall, Romain Mari, Guillaume Chatté, and Annie Colin, “Density waves in shear-thickening suspensions,” *Science Advances* **6**, eaay5589 (2020).
- [25] Brice Saint-Michel, Thomas Gibaud, and Sébastien Manneville, “Uncovering instabilities in the spatiotemporal dynamics of a shear-thickening cornstarch suspension,” *Phys. Rev. X* **8**, 031006 (2018).
- [26] Abdoulaye Fall, Anaël Lemaître, François Bertrand, Daniel Bonn, and Guillaume Ovarlez, “Shear thickening and migration in granular suspensions,” *Phys. Rev. Lett.* **105**, 268303 (2010).
- [27] Guillaume Ovarlez, François Bertrand, and Stéphane Rodts, “Local determination of the constitutive law of a dense suspension of noncolloidal particles through magnetic resonance imaging,” *Journal of rheology* **50**, 259–292 (2006).
- [28] Michiel Hermes, Ben M Guy, Wilson CK Poon, Guilhem Poy, Michael E Cates, and Matthieu Wyart, “Unsteady flow and particle migration in dense, non-brownian suspensions,” *Journal of Rheology* **60**, 905–916 (2016).
- [29] Endao Han, Ivo R. Peters, and Heinrich M. Jaeger, “High-speed ultrasound imaging in dense suspensions reveals impact-activated solidification due to dynamic shear jamming,” *Nature Communications* **7**, 12243 (2016).
- [30] Joachim Kaldasch, Bernhard Senge, and Jozua Laven, “Shear thickening in electrically-stabilized colloidal suspensions,” *Rheologica Acta* **47**, 319–323 (2008).
- [31] Joachim Kaldasch and Bernhard Senge, “Shear thickening in polymer stabilized colloidal suspensions,” *Colloid and Polymer Science* **287**, 1481–1485 (2009).
- [32] Vikram Rathee, Alessandro Monti, Marco E Rosti, and Amy Q Shen, “Shear thickening behavior in dense repulsive and attractive suspensions of hard spheres,” *Soft Matter* **17**, 8047–8058 (2021).
- [33] Qin Xu, Sayantan Majumdar, Eric Brown, and Heinrich M. Jaeger, “Shear thickening in highly viscous granular suspensions,” *Journal of Rheology* **64**, 321–328 (2020).

- lar suspensions,” *Europhysics Letters* **107**, 68004 (2014).
- [34] Romain Mari, Ryohei Seto, Jeffrey F. Morris, and Morton M. Denn, “Nonmonotonic flow curves of shear thickening suspensions,” *Phys. Rev. E* **91**, 052302 (2015).
- [35] Endao Han, Nicole M. James, and Heinrich M. Jaeger, “Stress controlled rheology of dense suspensions using transient flows,” *Phys. Rev. Lett.* **123**, 248002 (2019).
- [36] Ye Xu, Wilfried C. Engl, Elizabeth R. Jerison, Kevin J. Wallenstein, Callen Hyland, Larry A. Wilen, and Eric R. Dufresne, “Imaging in-plane and normal stresses near an interface crack using traction force microscopy,” *Proceedings of the National Academy of Sciences* **107**, 14964–14967 (2010).
- [37] Aaron F. Mertz, Shiladitya Banerjee, Yonglu Che, Guy K. German, Ye Xu, Callen Hyland, M. Cristina Marchetti, Valerie Horsley, and Eric R. Dufresne, “Scaling of traction forces with the size of cohesive cell colonies,” *Phys. Rev. Lett.* **108**, 198101 (2012).
- [38] Vikram Rathee, Daniel L. Blair, and Jeffrey S. Urbach, “Localized stress fluctuations drive shear thickening in dense suspensions,” *Proceedings of the National Academy of Sciences* **114**, 8740–8745 (2017).
- [39] Vikram Rathee, Daniel L. Blair, and Jeffrey S. Urbach, “Localized transient jamming in discontinuous shear thickening,” *Journal of Rheology* **64**, 299–308 (2020).
- [40] Weiwei Zhao, Jianhui Zhou, Haitao Hu, Chang Xu, and Qin Xu, “The role of crosslinking density in surface stress and surface energy of soft solids,” *Soft Matter* **18**, 507–513 (2022).
- [41] Vikram Rathee, Joia Miller, Daniel L Blair, and Jeffrey S Urbach, “Structure of propagating high-stress fronts in a shear-thickening suspension,” *Proceedings of the National Academy of Sciences* **119**, e2203795119 (2022).
- [42] Peter D. Olmsted, “Perspectives on shear banding in complex fluids,” *Rheologica Acta* **47**, 283–300 (2008).
- [43] Anaïs Gauthier, Mickaël Pruvost, Olivier Gamache, and Annie Colin, “A new pressure sensor array for normal stress measurement in complex fluids,” *Journal of Rheology* **65**, 583–594 (2021).